Computational Methods in Applied Sciences

João Manuel R. S. Tavares
R. M. Natal Jorge (Eds.)

Advances in Computational Vision and Medical Image Processing

Methods and Applications

Springer

ECCOMAS
European Community on Computational Methods in Applied Sciences

Computational Methods in Applied Sciences

Volume 13

Series Editor

E. Oñate
International Center for Numerical Methods in Engineering (CIMNE)
Technical University of Catalunya (UPC)
Edificio C-1, Campus Norte UPC
Gran Capitán, s/n
08034 Barcelona, Spain
onate@cimne.upc.edu
www.cimne.com

For other titles published in this series, go to
www.springer.com/series/6899

João Manuel R.S. Tavares · R.M. Natal Jorge
Editors

Advances in Computational Vision and Medical Image Processing

Methods and Applications

Springer

Editors

João Manuel R.S. Tavares

University of Porto (UP)
Faculty of Engineering (FEUP)
Institute of Mechanical Engineering
and Industrial Management (INEGI)
Rua Dr. Roberto Frias, s/n
4200-465 Porto
Portugal
tavares@fe.up.pt

R.M. Natal Jorge

University of Porto (UP)
Faculty of Engineering (FEUP)
Institute of Mechanical
Engineering (IDMEC)
Rua Dr. Roberto Frias, s/n
4200-465 Porto
Portugal
rnatal@fe.up.pt

ISBN: 978-1-4020-9085-1 e-ISBN: 978-1-4020-9086-8

Library of Congress Control Number: 2008934777

Printed on acid-free paper

springer.com

Preface

Computational methodologies of signal processing and imaging analysis, namely considering 2D and 3D images, are commonly used in different applications of the human society. For example, Computational Vision systems are progressively used for surveillance tasks, traffic analysis, recognition process, inspection purposes, human-machine interfaces, 3D vision and deformation analysis.

One of the main characteristics of the Computational Vision domain is its inter-multidisciplinary. In fact, in this domain, methodologies of several more fundamental sciences, such as Informatics, Mathematics, Statistics, Psychology, Mechanics and Physics are usually used. Besides this inter-multidisciplinary characteristic, one of the main reasons that contributes for the continually effort done in this domain of the human knowledge is the number of applications in the medical area. For instance, it is possible to consider the use of statistical or physical procedures on medical images in order to model the represented structures. This modeling can have different goals, for example: shape reconstruction, segmentation, registration, behavior interpretation and simulation, motion and deformation analysis, virtual reality, computer-assisted therapy or tissue characterization.

The main objective of the ECCOMAS Thematic Conferences on Computational Vision and Medical Image Processing (VIPimage) is to promote a comprehensive forum for discussion on the recent advances in the related fields trying to identify widespread areas of potential collaboration between researchers of different sciences.

The present book contains the extended versions of sixteen papers selected from the works presented in the first ECCOMAS thematic conference on Computational Vision and Medical Image processing (VIPimage 2007), held in Faculty of Engineering of University of Porto, Portugal. It collects the state-of-the-art on the subject of Computational Vision and Medical Image processing contributing for the development of these areas of knowledge.

The Editors would like to take this opportunity to thank to the European Community on Computational Methods in Applied Sciences, the Portuguese Association

of Theoretical, Applied and Computational Mechanics, the University of Porto, all sponsors, all members of the International Scientific Committee, and to all Invited Lecturers and Authors.

Faculty of Engineering,
University of Porto, Portugal

João Manuel R.S. Tavares
R. M. Natal Jorge

Contents

Chapter 12
Microscale Flow Dynamics of Red Blood Cells in Microchannels: An Experimental and Numerical Analysis

R. Lima, M. Nakamura, T. Omori, T. Ishikawa, S. Wada, and T. Yamaguchi

Abstract The blood flow dynamics in microcirculation depends strongly on the motion, deformation and interaction of red blood cells (RBCs) within the microvessel. We present confocal micro-PTV measurements on the motion of individual RBCs through a circular polydimethysiloxane (PDMS) microchannel. The RBC radial displacement and dispersion calculated from these measurements show that the RBC paths are strongly dependent on the both Hct and plasma layer. In order to obtain more detailed information of the non-Newtonian property of blood a novel computational scheme is also described. The simulated flow dynamics were in good agreement with the Casson flow model and *in vivo* observations. In the near future by comparing both results we hope to clarify a variety of complex phenomena occurring at the microscale level.

12.1 Introduction

Approximately, the half volume of the blood is composed of red blood cells (RBCs) which is believed to strongly influence its flow properties. Blood flow in microvessels depends strongly on the motion, deformation and interaction of RBCs. Several experimental studies on both individual and concentrated RBCs have already been performed in the past [3, 6–8]. However, all studies used conventional microscopes

R. Lima, T. Omori, T. Ishikawa, and T. Yamaguchi
Department of Bioengineering & Robotics, Graduate School Of Engineering, Tohoku University, 6-6-01 Aoba, 980-8579 Sendai, Japan

R. Lima
Department of Mechanical Technology, ESTiG, Bragança Polytechnic, C. Sta. Apolonia, 5301-857 Bragança, Portugal

M. Nakamura and S. Wada
Department of Mechanical Science and Bioengineering, Graduate School of Engineering, Osaka University, Toyonaka, 560-8531 Osaka, Japan

J.M.R.S. Tavares, R.M.N. Jorge (eds.), *Advances in Computational Vision and Medical Image Processing,* Computational Methods in Applied Sciences 13,

and also ghost cells to obtain visible trace RBCs through the microchannel. Recently, considerable progress in the development of confocal microscopy and consequent advantages of this microscope over the conventional microscopes have led to a new technique known as confocal micro-PIV [13, 15, 18, 21]. This technique combines the conventional PIV system with a spinning disk confocal microscope (SDCM). Due to its outstanding spatial filtering technique together with the multiple point light illumination system, this technique has the ability to obtain in-focus images with optical thickness less than 1 μm.

In a numerical context, blood flow in large arteries is usually modeled as a continuum however this assumption is not valid in small vessels such as arterioles and capillaries. In this way, we are developing an integrative multi-scale model to simulate the blood flow at mesoscopic level. This computational approach may provide important information on the rheology of blood in small vasculatures where non-Newtonian property of blood is not negligible.

The main purpose of this paper is to measure flow behavior of individual RBCs at different haematocrits (Hct) through a 75 μm circular polydimethysiloxane (PDMS) microchannel by means of confocal micro-PTV system. Moreover we introduce an integrative multi-scale model to simulate the blood flow behavior through microvessels in order to obtain more detailed insights about the blood rhelogical properties at cellular level.

12.2 Confocal Micro-PTV Measurements of RBCs

12.2.1 Materials and Methods

12.2.1.1 Working Fluids and Microchannel

Four working fluids were used in this study: dextran 40 (Dx40) containing about 3% (3 Hct), 13% (13 Hct), 23% (23 Hct) and 37% (37 Hct) of human RBCs. The blood was collected from a healthy adult volunteer, where ethylenediaminetetraacetic acid (EDTA) was added to prevent coagulation. The RBCs where separated from the bulk blood by centrifugation (1,500 RPM for 5 min) and aspiration of the plasma and buffy coat and then washed twice with physiological saline (PS). The washed RBCs were labeled with a fluorescent cell tracker (CM-Dil, C-7000, Molecular Probes) and then diluted with Dx40 to make up the required RBCs concentration by volume [10, 12]. All blood samples were stored hermetical at 4 °C until the experiment was performed at controlled temperature of about 37 °C. All procedures in this experiment were carried out in compliance with the Ethics Committee on Clinical Investigation of Tohoku University.

By using a soft lithography technique it is possible to fabricate easily precise and reproducible rectangular microchannels at low cost. Rectangular PDMS microchannel with a low aspect ratio seems to be appropriate to perform confocal micro-PIV measurements of *in vitro* blood [14]. However, this geometry may not reflect the

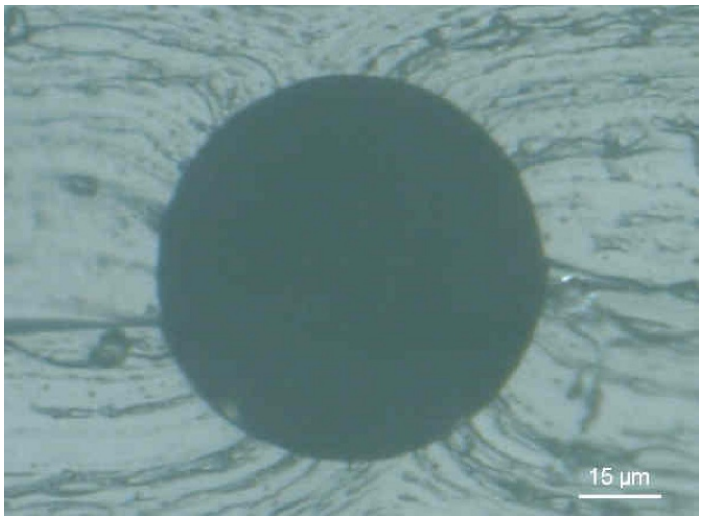

Fig. 12.1 Cross section of the PDMS microchannel

actual physiology of the microcirculation. Hence, very recently we have successfully fabricated straight circular PDMS microchannels by using a wire casting technique [12]. The microchannel used in this study was a PDMS circular microchannel with a diameter of 75 µm (Fig. 12.1).

12.2.1.2 Confocal Micro-PTV Experimental Set-Up

The confocal micro-PIV system used in our experiment consists of an inverted microscope (IX71, Olympus, Japan) combined with a confocal scanning unit (CSU22, Yokogawa, Japan) and a diode-pumped solid state (DPSS) laser (Laser Quantum Ltd, UK) with an excitation wavelength of 532 nm. Moreover, a high-speed camera (Phantom v7.1, Vision Research, USA) was connected into the outlet port of the CSU22 (see Fig. 12.2). The PDMS microchannel was placed on the stage of the inverted microscope where the flow rate of the working fluids was kept constant $(\mathrm{Re} \sim 0.004)$ by means of a syringe pump (KD Scientific Inc., USA). A thermo plate controller was set to 37 °C. All the confocal images were captured in the middle of the microchannels with a resolution of 640×480 pixels, at a rate of 100 frames/s with an exposure time of 9.4 ms. The recorded images were transferred to the computer and then evaluated in Image J (NIH) [1] by using a manual tracking MTrackJ [16] plugin. As a result it was possible to track single RBCs through the middle plane of the PDMS microchannel.

12.2.1.3 RBC Radial Displacement and Radial Dispersion Coefficient

The radial displacements $(\Delta \mathrm{R})$ of the tracked RBCs were determined by using the following equation:

$$\Delta R(t) = |R(t_0 + t) - R(t_0)| \tag{12.1}$$

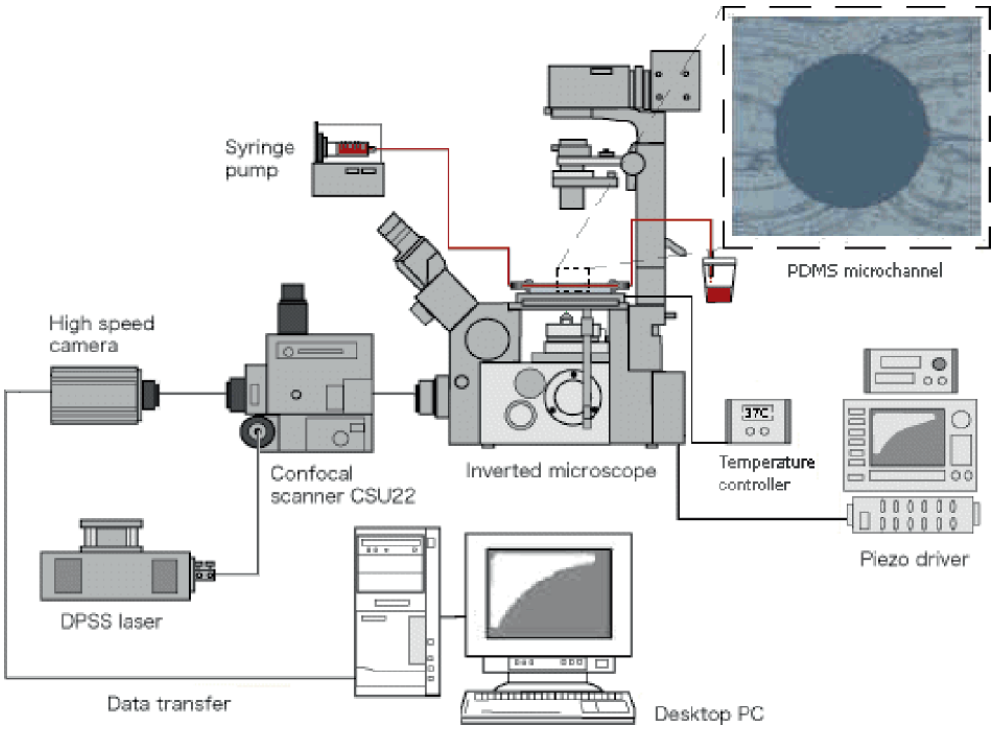

Fig. 12.2 Experimental set-up

where R(t) is the radial position at time t, t_0 is the initial time, and $\Delta R(t)$ is the radial displacement at time interval t.

Besides the calculation of the radial displacement (ΔR), we have also analyzed the motions of RBCs by using a radial dispersion coefficient (D_{yy}) [8,9], given by:

$$D_{yy}(t) = \frac{1}{N}\sum_{i=1}^{N}\frac{\left\langle (R_{i,y}(t) - R_{i,y}(0))^2 \right\rangle}{2t} \tag{12.2}$$

where R, t, N are the radial displacement, time interval and number of RBCs respectively.

12.2.2 Results and Discussion

12.2.2.1 Blood Flow Visualization at Several Hcts

Figure 12.3 shows images with both non-labeled RBCs (halogen illumination) and labeled RBCs (laser-emitted light) measured in centre plane of 75 µm circular PDMS microchannel at several Hcts (from 3% to 37%) with Re from 0.004 to 0.005.

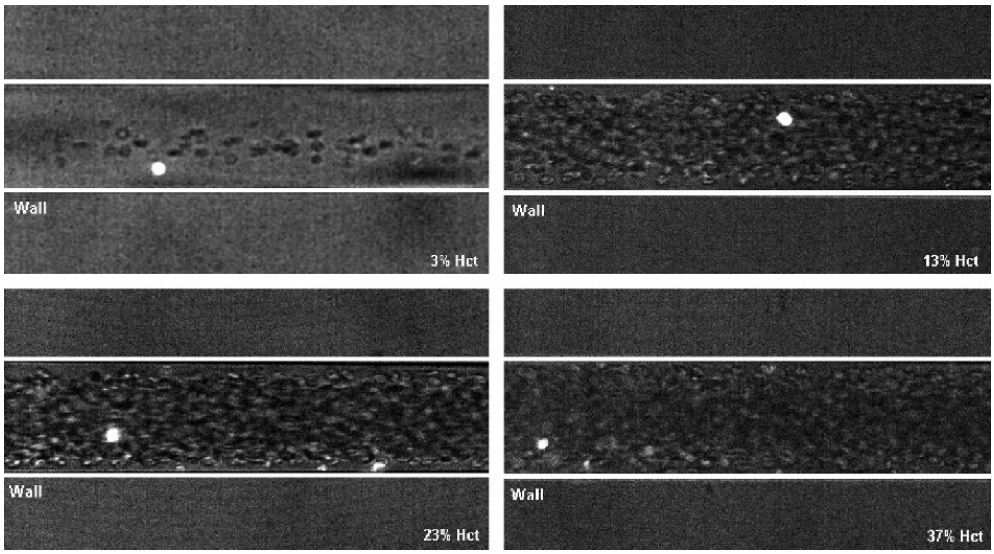

Fig. 12.3 Both normal and labeled rbcs (bright spots) with 3% Hct, 13% Hct, 23% Hct, 37% Hct (20×, 1.6 zoom)

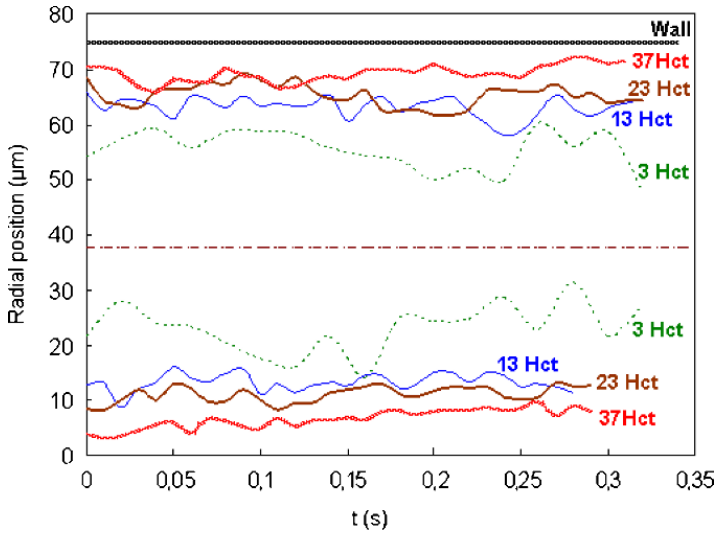

Fig. 12.4 The effect of the Hct on the plasma layer

From Fig. 12.3 it is possible to observe that the Hct decreases with the microchannel diameter which corroborates with the well known Faharaeus effect [3]. Moreover, it is also evident that the plasma layer tends to increase by decreasing the Hct (see Figs. 12.4 and 12.5). This latter phenomenon is related to the Fahareues-Lindqvist effect [5]. Although this phenomenon is still not completely understood [2], the most acceptable explanation is related to the tendency of the RBCs to migrate toward the microtube axis enhanced by the RBCs deformation and interations [6, 19]. A further consequence is that the apparent blood viscosity is reduced so that the flow resistance through the capillary also decreases.

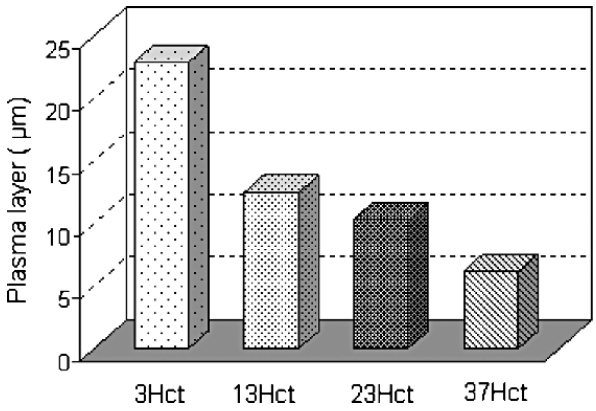

Fig. 12.5 Average thickness of the plasma layer at several Hcts

12.2.2.2 Radial Displacement in a 75 μm PDMS Microchannel

Figure 12.6a shows the effect of the radial position on the motion of labeled RBCs flowing through a 75 μm PDMS capillary, for a feed Hct of about 13%. In addition Fig. 12.6b shows the radial displacement of a RBC flowing through microchannel with Hct of about 3%. The correspondent radial displacements (ΔR) are shown in Fig. 12.7.

From Fig. 12.7 it is clear that the RBCs radial displacement (ΔR) for 13% Hct is higher than a RBC flowing within an Hct of 3%. In addition it is also possible to observe that the radial displacement (ΔR) of the RBC flowing close to the plasma layer (12 μm from the wall) is around three times higher than the RBC (36 μm from the wall) traveling around the middle of the microchannel. These results suggest that RBCs flowing within the boundary region of RBC core appear to undergo the largest radial displacements. We believe that the random like transverse motions happening in this region are mainly due to multiple hydrodynamic interactions with neighboring RBCs which flow with lower velocity adjacent to the wall or tend to migrate away from the microtube wall towards the RBC core region.

12.2.2.3 Radial Dispersion in 75 μm PDMS Microchannel at Several Hcts

By measuring the radial displacement of labeled RBCs flowing through the microchannel for a known time interval, it was possible to calculate the correspondent dispersion coefficient (D_{yy}). Figure 12.8 shows the RBC averaged dispersion coefficient at the middle plane (D_{yy}) for several Hcts (3% Hct, 13% Hct, 23% Hct and 37% Hct).

Figure 12.8 shows that the radial dispersion coefficient (D_{yy}) increases with the Hct. The RBC D_{yy} for Hcts from 23% to 37% have almost one order of magnitude greater than the D_{yy} with 3% Hct. These results clearly reflect the RBCs radial displacement obtained in Fig. 12.7.

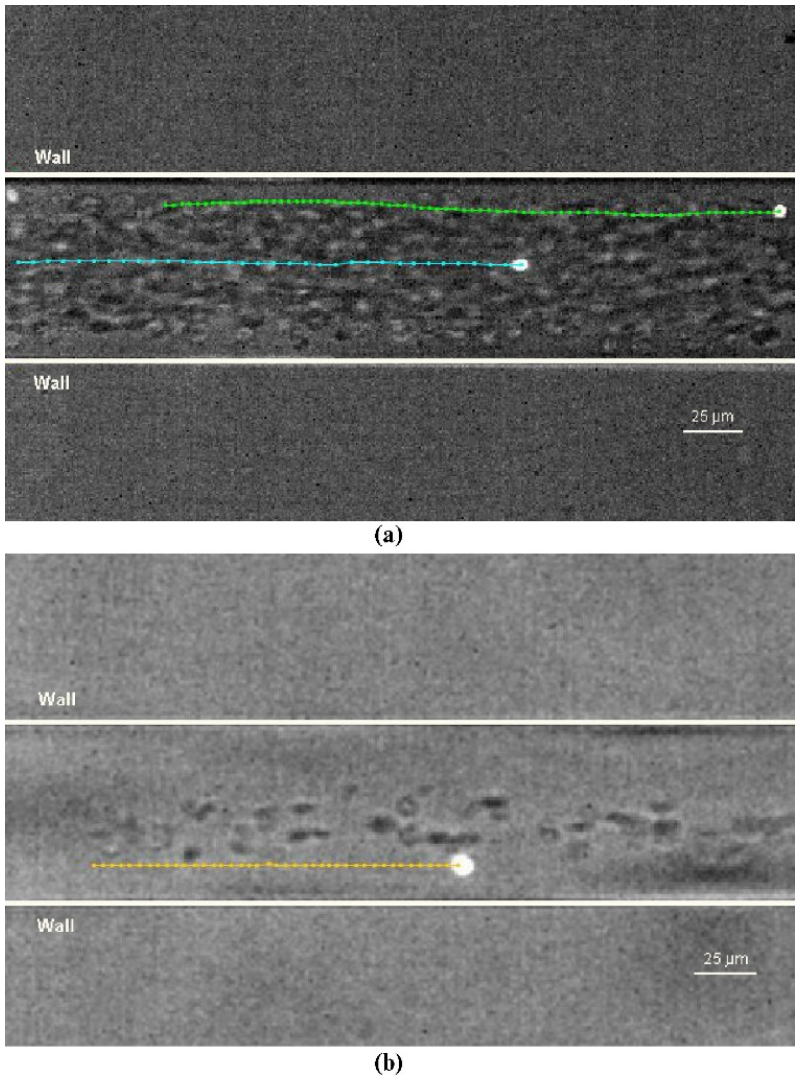

Fig. 12.6 Rbcs streamlines at several haematocrits: (**a**) 13% Hct, (**b**) 3% Hct

Generally, our results demonstrate that the RBCs at dense concentrations exhibit higher erratic radial displacement when compared with diluted suspensions of RBCs. Although it is evident that the RBC radial dispersion rises with the increase of Hct at Hcts of about 24% it tends to level off (see Fig. 12.9). Note that, these observations are consistent with several other measurements performed in glass microchannels [8, 11].

The results from Fig. 12.10 reinforce our previous measurements obtained from glass capillaries [11]. These data clearly demonstrate that RBC radial dispersion tend to decrease with the diameter. We believe that the main reason is due not only to Hct reduction with the diameter (Faharaeus effect) but also to the geometry constriction which limits the amplitude of the RBCs radial displacements.

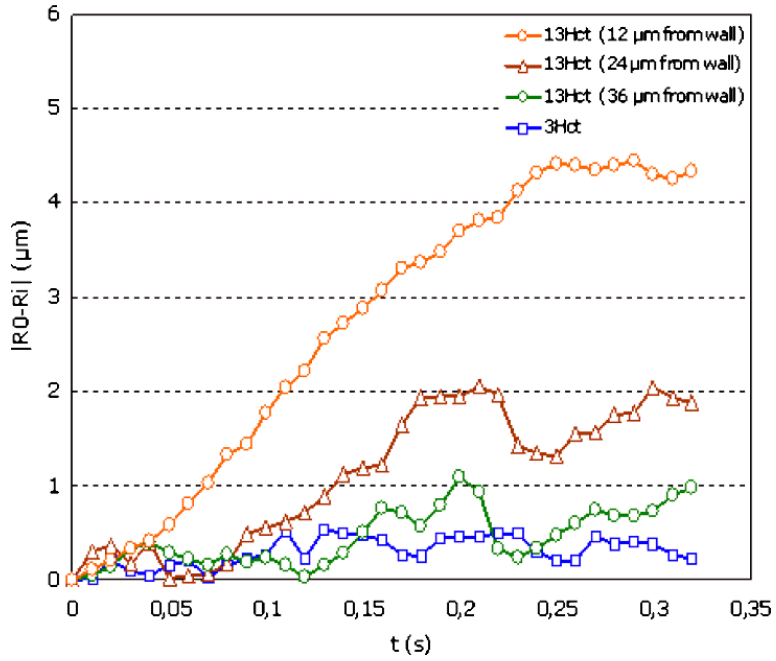

Fig. 12.7 Radial displacement (ΔR) of labeled rbcs at several haematocrits (3% Hct and 13% Hct) and at different radial positions

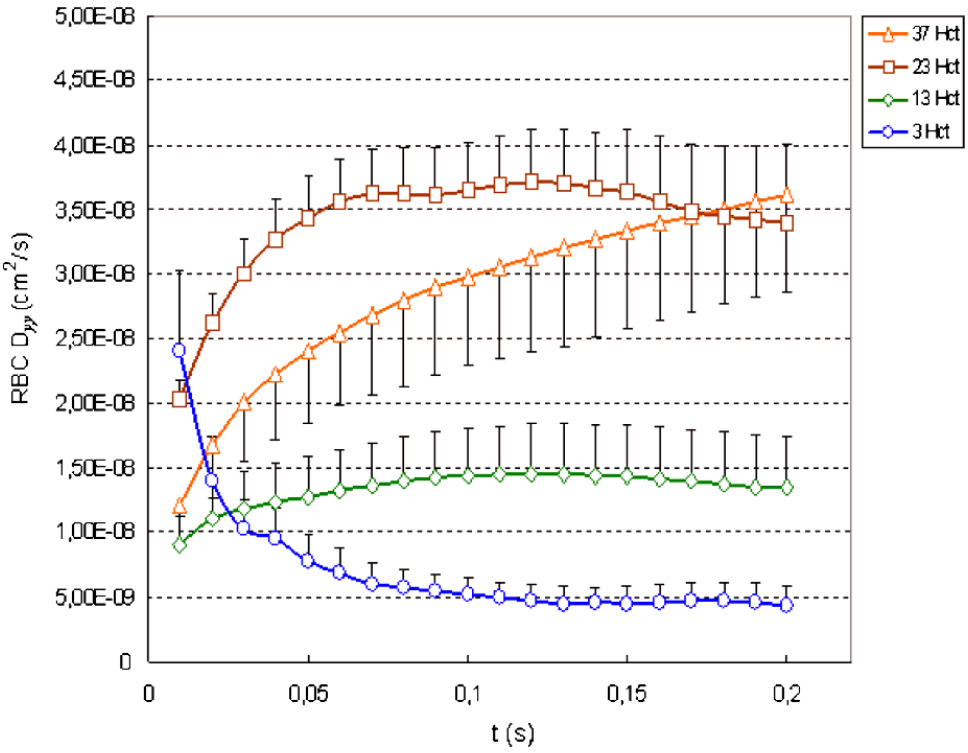

Fig. 12.8 RBC averaged dispersion coefficient at the middle plane (D_{yy}) for several Hcts: 3% Hct, 13% Hct, 23% Hct and 37% Hct

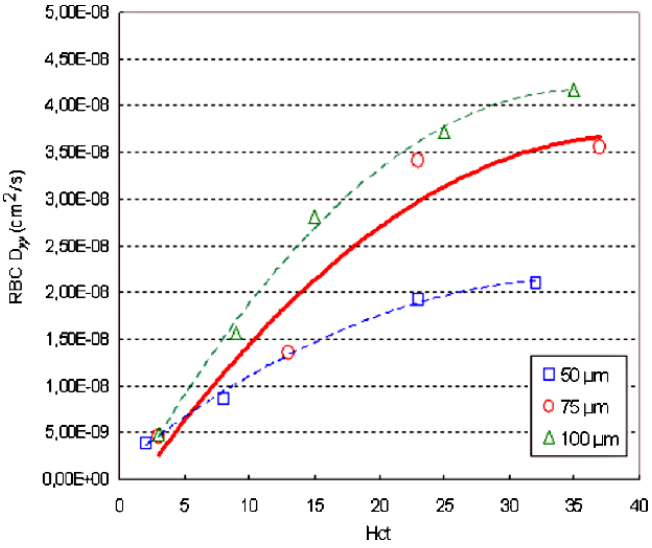

Fig. 12.9 Effect of the Hct on the RBC D_{yy} at 75 µm PDMS microchannel and 100 µm, 50 µm glass capillary [11]

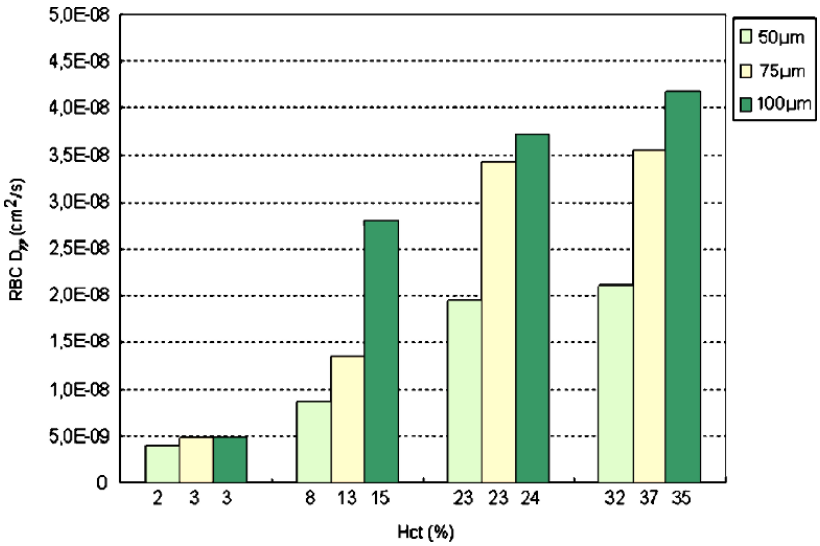

Fig. 12.10 The effect of the microchannel diameter on the RBC D_{yy}

12.3 Numerical Flow Model of Multiple RBCs

A simulation method for multiple RBCs in a micro-vasculature was proposed for understanding the rheological properties of blood from a viewpoint of multiscale mechanics. In the following context, blood flow is modeled at two different scales. A micro-scale flow is modeled as a particulate flow of RBCs. On the other hand, flow at a macro-scale is modeled as a continuum expressed by the equations of continuity and Navier-Stokes. Then, a coupling method between those differently-scaled blood flow models is described. Finally, the simulation results are presented.

12.3.1 Materials and Methods

12.3.1.1 Microscale Blood Flow Model (RBC Flow Model)

An RBC model developed by Wada and Kobayashi [22] was adopted. This model is capable of expressing a biconcave shape of the RBC at rest as well as its elastic deformation while in motion. As shown in Fig. 12.11, the model was constructed by surrounding the internal liquid of RBC with RBC membrane consisting of N nodal points linked by a spring element.

Owing to deformation, elastic energies are generated and stored in RBC. The stretching energy W_s and bending energy W_b are modeled as

$$W_s = \frac{1}{2} k_s \sum_{l=1}^{N} (L_l - L_{l0})^2 \tag{12.3}$$

$$W_b = \frac{1}{2} k_b \sum_{l=1}^{N_l} L_l \tan^2 \left(\frac{\theta_l}{2} \right) \tag{12.4}$$

where k_s and k_b are spring constants, N, N_1 are the number of nodes and lines, L_{l0}, L_l are length of spring at the natural state and after deformation, θ_l is the contacting angle between neighboring elements. To maintain the total area of RBC (actually it is volume in 3D), a penalty functions W_A was introduced. Mathematically, it was defined by

$$W_A = \frac{1}{2} k_A \left(\frac{A - A_0}{A_0} \right)^2 A_0, \tag{12.5}$$

where subscript 0 denotes the natural state, N_e is the number of bending springs, k_a is a coefficient for the area constraint.

An interactive force working between two RBCs which come closer are expressed by a potential function Ψ assigned at each nodal point on the RBC membrane. The potential function Ψ for nodal point i is a summation of interactive forces from all neighboring nodal points as formulated by

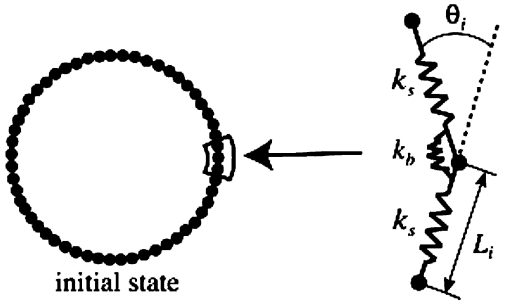

Fig. 12.11 Red blood cell model. Nodal points on the membrane were connected by a mechanical spring. The neighboring springs were also linked by a bending spring

$$\Psi = \sum_{j=1}^{N} \Psi_{ij} \tag{12.6}$$

where Ψ_{ij} is the potential function on nodal point i from nodal point j on neighboring RBC. It is given by

$$\Psi_{ij} = \begin{cases} k_r \left(\frac{\pi z_{ij}}{2} - \tan\left(\frac{\pi z_{ij}}{2} \right) \right) & for \quad -1 \le z_{ij} \le 0 \\ 0 & for \quad 0 \le z_{ij} \end{cases} \tag{12.7}$$

where $z_{ij} = d_{ij}/\delta - 1$, d_{ij} is a distance between nodal points i and j, and δ is equilibrium distance. According to this function, a repulsive force acts when they are come much closer. In the present simulation, the equilibrium distance δ is set to L_0 which is natural length of a spring.

An interactive force working between an RBC and a vessel wall is modeled in a way similar to the interactive force between two RBCs. The potential function Z for nodal point i is expressed by a summation of interactive forces from all neighboring nodal points as formulated by

$$\mathrm{Z} = \sum_{i=1}^{N} \mathrm{Z}_i \tag{12.8}$$

where Z_i is the potential function on nodal point i from nodal point j on neighboring RBC, which is given by

$$Z_i = \begin{cases} k_w \left(\frac{\pi z_i}{2} - \tan\left(\frac{\pi z_i}{2} \right) \right) & for -1 \le z_i \le 0 \\ 0 & for \quad 0 \le z_i \end{cases} \tag{12.9}$$

where $z_i = D_i/\delta_w - 1$, D_i is the distance between nodal point i and the wall, k_w is a parameter to express the magnitude of a repulsive force, and δ_w is an equilibrium distance. Here, δ_w was set to the same as δ.

Modeling of a fluid force $\mathbf{f_i}$ working on an RBC is made separately for forces $\mathbf{f}_{ni}$ and $\mathbf{f}_{ti}$ which respectively work in normal and tangential directions to a line element i of an RBC membrane. On the basis of the conservation of momentum, the normal force, $\mathbf{f}_{ni}$ working on a line element i of the RBC membrane is modeled as

$$\mathbf{f}_{ni} = \rho L_i \mathbf{v}_{ni}^2 \tag{12.10}$$

where ρ is a density of plasma, and $\mathbf{v}_{ni}$ is a normal component of the velocity difference between an RBC and a plasma flow. The tangential force $\mathbf{f}_t$ is modeled based on Newton's law of viscosity. If we assume that a flow velocity at a distance Δ from an RBC membrane is the same as a flow velocity at the RBC membrane, the tangential force $\mathbf{f}_{ti}$ that works on a line element i can be approximated as

$$\mathbf{f}_{ti} = \mu_p L_i \, \mathbf{v}_{ti}/\Delta \tag{12.11}$$

where μ_p is a viscosity of plasma, $\mathbf{v}_{ti}$ is a tangential component of $\mathbf{v}_i$. The equivalent distance Δ in Eq. (12.11) was estimated from Oseen flow theory where a

two-dimensional cylinder with a radius of a falls down in a viscous fluid. The distance Δ is therefore

$$\Delta = \left(2.0\left(\ln\frac{8.0}{\mathrm{Re}} - \gamma\right) + 1.0\right)\frac{a}{8.0} \tag{12.12}$$

where Re is the Reynolds number determined from a relative velocity of the cylinder to a fluid and a diameter of the cylinder and γ is Euler constant $(= 0.57721)$. In the present study, a is set to be comparable to the size of an RBC. Note that the fluid force is assumed not to work when a distance between two RBCs is less than δ for presuming the situation that they are in touch.

Given elastic energies and fluid forces, the motion of nodal point i placed on RBC membrane was determined from

$$m\ddot{\mathbf{r}}_i + \gamma(\dot{\mathbf{r}}_i - \dot{\mathbf{r}}_g) = \mathbf{F}_i + \mathbf{f}_i \tag{12.13}$$

where a dot means a time derivative, $\mathbf{r}_i$ is the position vector of nodal point i, m is mass of the nodal point, and $\mathbf{f}_i$ is a fluid force $(= \mathbf{f}_{ti} + \mathbf{f}_{ni})$. Based on the virtual work theory, an elastic force $\mathbf{F}_i$ is given by

$$\mathbf{F}_i = \frac{\partial W}{\partial r_i} \tag{12.14}$$

$$W = W_s + W_b + W_a + \Psi + \mathrm{Z}. \tag{12.15}$$

12.3.1.2 Macroscale Blood Flow Model (Continuum Flow Model)

A macroscale blood flow at a steady state is modeled as a continuum expressed by the Navier-Stokes and continuity equations;

$$u_j\frac{\partial u_i}{\partial x_j} = -\frac{\partial p}{\partial x_i} + \frac{\partial}{\partial x_j}\left[\frac{1}{\mathrm{Re}}\left(\frac{\partial u_i}{\partial x_j} + \frac{\partial u_j}{\partial x_i}\right)\right] \tag{12.16}$$

$$\frac{\partial u_i}{\partial x_i} = 0 \tag{12.17}$$

where u_i is a flow velocity component and p is a pressure. In general, fluid viscosity is assumed to be spatially constant for the analysis of arterial blood flow. However, it is not true in small arteries due to spatial variation of RBC concentration. We here introduce a Hematocrit function $F(\mathrm{Hct})$ to the viscous term of the Navier-Stokes equation in order to express a local viscosity dependent on a local hematocrit.

Blood flow is often represented by Casson model. Shiga et al. [20] obtained an empirical formula of the relationship between Casson viscosity η_c and hematocrit Hct as

$$\ln\left(\frac{\eta_c}{\eta_p}\right) = k \cdot \mathrm{Hct} \tag{12.18}$$

where η_p is a plasma viscosity and k is a constant. Based on this equation, we express the hematocrit function F as

$$F = \frac{\eta_c}{\eta_p} = \exp\left[k \cdot \mathrm{Hct}\right], \tag{12.19}$$

whereby the Navier-Stokes equation is rewritten as

$$u_j \frac{\partial u_i}{\partial x_j} = -\frac{\partial p}{\partial x_i} + \frac{\partial}{\partial x_j}\left[\frac{\exp\left[k \cdot \mathrm{Hct}\right]}{\mathrm{Re}}\left(\frac{\partial u_i}{\partial x_j} + \frac{\partial u_j}{\partial x_i}\right)\right] \tag{12.20}$$

In the actual simulation of a macroscale flow, we solve Eqs. (12.17) and (12.20) by a finite element method.

12.3.1.3 Geometry Model of a Small Vasculature

The present study solved blood flowing between a two-dimensional parallel plate flow channel. The x-axis and y-axis were respectively set in axial and radial directions of the channel. For the microscale simulation, 108 RBCs were put in the channel with height of 96 μm and length of 44 μm. In this case, Hct is 0.31. A periodic boundary condition was assumed for both x-ends of the channel. For the macroscale flow analysis, the channel is extended to 480 mm. The flow region was divided into triangular finite elements. The total numbers of nodal points and elements were 2,500 and 4,752, respectively.

12.3.1.4 Simulation Condition

Table 12.1 encapsulates the parameter of the microscale flow. The Reynolds number was 0.6. Parameter k in Eq. (12.19) was set to 2.85 based on the viscosity of the whole blood of 4.55 mPa · s and that of the plasma of 1.33 mPa · s at Hct of 0.44, a shear rate of 230 s^{-1}, and temperature of 37 °C.

Table 12.1 Parameters used for the simulation

Number of nodes, N	60
Mass, m	1.0×10^{-15} kg
Spring constant for stretching, k_s	1.0×10^{-17} J
Spring constant for bending, k_b	1.0×10^{-18} J
Spring constant for the area constraint, k_a	1.0×10^{-16} J
Viscosity of the red blood cell membrane, γ	1.0×10^{-10} kg/s

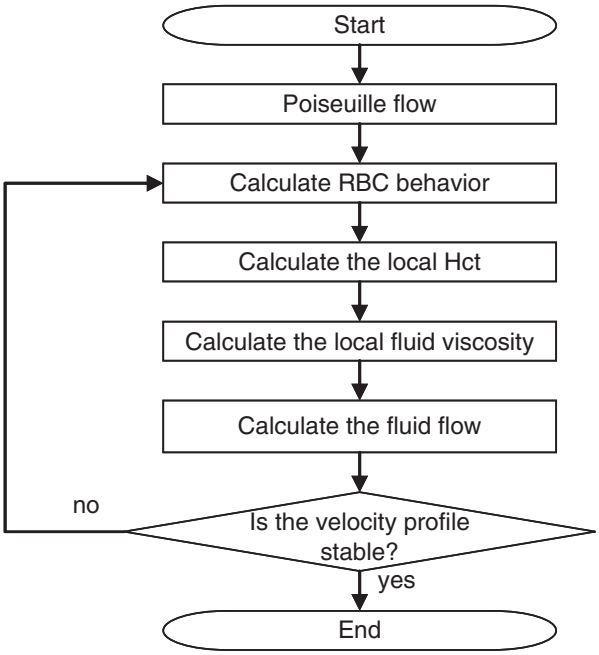

Fig. 12.12 Flowchart of the present simulation

12.3.1.5 Simulation Procedure

A flowchart of the simulation is shown in Fig. 12.12. Assuming with Poiseuille flow as an initial axial flow, the microscale flow is calculated. When the radial distribution of RBCs becomes stable, the calculation is stopped, and the Hct functions are obtained for flow segments defined by radially subdividing the flow channel by N to incorporate the influence of the local variation of an RBC distribution into the macroscale flow analysis. The macroscale flow simulation is performed until a fully-developed axial velocity profile is obtained. With this velocity profile, the simulation is back to the microscale simulation. This process is repeated until a change in the axial velocity profile after the microscale flow simulation is negligible. In the present simulation, $N = 8$.

12.3.2 Result

The results showed a drastic change in the distribution of RBCs with progress of the simulation. The spatial distributions of RBCs at the initial state and the converged state are shown in Fig. 12.13. On the right of each figure, the percentage of RBCs in each flow segment at each state is plotted. At the initial state, RBCs were distributed almost uniformly in a radial direction and were found near the wall the initial state. As RBCs were carried downstream by a fluid flow, they inclined and migrated to the center of the flow channel. As a result, RBCs were concentrated around the center and barely found near the wall, forming a plasma layer.

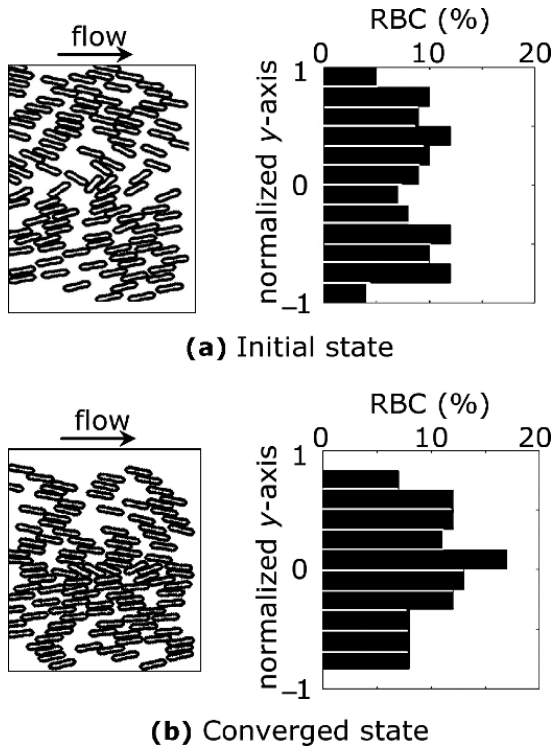

Fig. 12.13 Comparison of RBC distribution between the initial state (**a**) and the converged state (**b**)

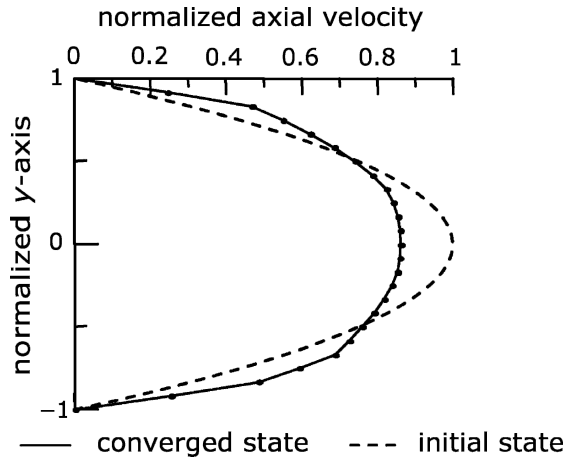

Fig. 12.14 Comparison of the axial velocity profile between the initial and converged states

The axial velocity profiles at the initial and converged states are depicted in Fig. 12.14. At the initial state, the velocity profile was parabolic as given. With progress of the simulation, there was a tendency that velocity at the center of the flow channel decreased while that near the wall increased. At the converged state, the axial flow took a rather flat velocity profile as seen in Fig. 12.14. The maximal velocity at the converged state decreased by 13.7% compared to that of the Poiseuille flow.

12.3.3 Discussion

A blood flow property in a small vasculature was analyzed by interactively simulating macro- and micro-scale blood dynamics. The results of the microscale flow simulation showed that RBCs gathered around the center of the flow channel and a plasma layer near the wall at the converged state. On the other hand, the macroscale flow showed a flat velocity profile. These flow features are quite similar to the in vivo observations [4, 17]. It is therefore considered that the simulation results represent the process of how the microscopic flow influences the macroscopic flow.

It is quite obvious that RBC behavior induced a flat velocity profile of the macroscale flow and *vice versa*. With an axial migration of RBCs, the RBC concentration became higher around the center of the channel while that near the wall became less, bringing about an increase in blood viscosity around the center and the decrease near the wall, respectively. As a consequence, the flow velocity around the center of the channel decreased and that near the wall increased, developing into a flat velocity profile.

12.4 Conclusions

Quantitative description of the flow behavior of labeled RBCs in both diluted and concentrated suspensions were studied under a confocal micro-PTV system. The experiments were performed in the middle plane of 75 μm circular PDMS microdevice at low Reynolds numbers $(\mathrm{Re} \sim 0.004)$ by using Hcts from 3% up to 37%. Our experimental results suggest that the RBC paths are strongly dependent on the Hct and as a result both RBC radial displacement and RBC radial dispersion increase with the heamatocrict. Moreover, our results also indicate that RBCs flowing around the plasma layer appear to undergo the largest radial displacements. The confocal micro-PTV system used in the present work is proved to be a powerful technique to measure the motion of labeled RBCs at different Hcts through a circular PDMS microchannel.

A novel computational scheme for the analysis of the mesoscopic blood rheology was proposed. The scheme was applied for the analysis of blood flow in a small vasculature. The simulated flow dynamics were in good agreement with the Casson flow model and *in vivo* observations. These results addressed the potential of the present computational approach to the analysis of the rheology of blood in small vasculatures where non-Newtonian property of blood is significant.

By comparing both results we hope in the near future to clarify a variety of complex phenomena occurring at the microscale level.

Acknowledgements This study was supported in part by the following grants: International Doctoral Program in Engineering from the Ministry of Education, Culture, Sports, Science and Technology of Japan (MEXT), “Revolutionary Simulation Software (RSS21)” next-generation IT program of MEXT; Grants-in-Aid for Scientific Research from MEXT and JSPS Scientific

Research in Priority Areas (768) "Biomechanics at Micro- and Nanoscale Levels, Scientific Research (S) No. 19100008, Grant-in-Aid for Young Scientists (A) 19680024.

References

1. Abramoff M., Magelhaes P., Ram S. (2004) Image Processing with Image Journal of Biophotonics International 11: 36–42.
2. Caro C., Pedley, T., Schroter R., Seed W. (1978) The mechanics of the circulation. Oxford, Oxford University Press.
3. Chien S., Usami S., Skalak R. (1984) Blood flow in small tubes In: Handbook of physiology – the cardiovascular system IV, Microcirculation, Part I. Bethesda MD, American Physiological Society, pp 217–249.
4. Cloutier G., Qin Z., Durand L.G., Teh B.G. (1996) Power Doppler ultrasound evaluation of the shear rate and shear stress Dependences of red blood cell aggregation. IEEE Transactions on Biomedical Engineering 43: 441–450.
5. Fahraeus R., Lindqvist T. (1931) The viscosity of the blood in narrow capillary tubes. American Journal of Physiology 96: 562–568.
6. Goldsmith H. (1971) Red cell motions and wall interactions in tube flow. Federation Proceedings 30: 1578–1588.
7. Goldsmith H., Marlow J. (1979) Flow behavior of erythrocytes. II. Particles motions in concentrated suspensions of ghost cells. Journal of Colloid and Interface Science 71: 383–407.
8. Goldsmith H., Turitto V. (1986) Rheological aspects of thrombosis and haemostasis: basic principles and applications. ICTH-Report-Subcommittee on Rheology of the International Committee on Thrombosis and Haemostasis. Thrombosis and Haemostasis 55: 415–435.
9. Ishikawa T., Pedley T. (2007) Diffusion of swimming model micro-organisms in a semi-dilute suspensions. Journal of Fluid Mechanics 588: 437–462.
10. Lima R., Ishikawa T., Imai, Y., Takeda, M., Wada, S., Yamaguchi, T. (2008a) "Measurement of individual red blood cell motions under high hematocrit conditions using a confocal micro-PTV system" (under revision to Annals of Biomedical Engineering).
11. Lima R., Ishikawa T., Imai, Y., Takeda, M., Wada, S., Yamaguchi, T. (2008) Radial dispersion of red blood cells in blood flowing through glass capillaries: role of hematocrit and geometry. Journal of Biomechanics 41: 2188–2196.
12. Lima R. (2007) Analysis of the blood flow behavior through microchannels by a confocal micro-PIV/PTV system. Ph.D. thesis, Tohoku University, Japan.
13. Lima, R., Wada, S., Takeda, M., Tsubota, K., Yamaguchi, T. (2007) In vitro confocal micro-PIV measurements of blood flow in a square microchannel: the effect of the haematocrit on instantaneous velocity profiles. Journal of Biomechanics 40: 2752–2757.
14. Lima, R., Wada, S., Tanaka, S., Takeda, M., Ishikawa, T., Tsubota, K., Imai, Y., Yamaguchi, T. (2008) In vitro blood flow in a rectangular PDMS microchannel: experimental observations using a confocal micro-PIV system. Biomedical Microdevices 10: 153–167.
15. Lima, R., Wada, S., Tsubota, K., Yamaguchi, T. (2006) Confocal micro-PIV measurements of three dimensional profiles of cell suspension flow in a square microchannel. Measurement Science and Technology 17: 797–808.
16. Meijering E., Smal I., Danuser G. (2006) Tracking in molecular bioimaging. IEEE Signal Processing Magazine 23: 46–53.
17. Oka S. (1984) Biorehology. Shokabo, Tokyo.
18. Park J., Choi C., Kihm K. (2004) Optically sliced micro-PIV using confocal laser scanning microscopy (CLSM). Experiments in Fluids 37: 105–119.
19. Schmid-Schonbein, H., Wells, R. (1969) Fluid drop-like transition of erythrocytes under shear. Science 165: 288–291.
20. Shiga T., Maeda N., Suda T., Kon K., Sekiya M., Oka S. (1979) Rheological and kinetic dysfunctions of the cholesterol-loaded, human erythrocytes. Biorheology 16: 363–369.

21. Tanaami T., Otsuki S., Tomosada N., Kosugi Y., Shimizu M., Ishida H. (2002) High-speed 1-frame/ms scanning confocal microscope with a microlens and Nipkow disks. Applied Optics 41: 4704–4708.
22. Wada S., Kobayashi R. (2003) Numerical simulation of various shape changes of a swollen red blood cell by decrease of its volume. Transactions of the Japan Society of Mechanical Engineers 69A: 14–21 (in Japanese).